Hydrogen Embrittlement Cracking Produced by Indentation Test

8

Akio Yonezu and Xi Chen

Contents

Abstract

Indentation is a convenient method to evaluate mechanical properties of materials as well as to simulate contact fracture with locally plastic deformation. Indentation experiment has been widely used for brittle solids, including ceramics and glass, for evaluating the fracture properties. With the aid of computational framework, simulation of crack propagation (for quasi-static and dynamic impact) is conducted to characterize "brittleness" of materials. In this review, we explore the applicability of indentation method for hydrogen embrittlement

A. Yonezu (✉)
Department of Precision Mechanics, Chuo University, Tokyo, Japan
e-mail: yonezu@mech.chuo-u.ac.jp

X. Chen
Department of Earth and Environmental Engineering, Columbia Nanomechanics Research Center, Columbia University, New York, NY, USA
e-mail: xichen@columbia.edu

G. Z. Voyiadjis (ed.), *Handbook of Nonlocal Continuum Mechanics for Materials and Structures*, https://doi.org/10.1007/978-3-319-58729-5_23

cracking (HEC). HEC is an important issue in the development of hydrogen-based energy systems. Especially high-strength steels tend to suffer from HE cracking, which leads to a significant decrease in the mechanical properties of the steels, including the critical stress for crack initiation and resistance to crack propagation. For such materials integrity for HEC, convenient material testing is necessary. In this review, the first part describes new indentation methodology to evaluate threshold stress intensity factor K_{ISCC}, and the latter one is investigation into HEC morphology due to residual stress produced by indentation impression. Our findings will be useful for predicting K_{ISCC} for HE instead of conventional long-term test with fracture mechanics testing. It will also indicate the stress criterion of HE cracking from an indentation impression crater, when the formed crater (for instance due to shot peening or foreign object contact) is exposed to a hydrogen environment.

Keywords
Indentation · Hydrogen embrittlement cracking · Fracture strength · Finite element method · Cohesive zone model · Residual stress · High-strength steel

Introduction

Hydrogen embrittlement (HE) cracking is an important issue in the development of hydrogen-based energy systems. High-strength steels tend to suffer from HE cracking, which leads to a significant decrease in the mechanical properties of the steels, including the critical stress for crack initiation and resistance to crack propagation. It is well known that Mode-I tensile stress is responsible for HE cracking (Gangloff 2003). In contrast, degradation of the mechanical properties upon compression loading (e.g., macroscopic hardness) never occurs in a hydrogen environment (Reddy et al. 1992). In order to evaluate the structural integrity of the material with respect to hydrogen embrittlement, tensile or bending loading is usually employed for mechanical testing, producing tensile stress for HE cracking. In contrast, we found that Vickers indentation caused HE cracking in high-strength steel (Yonezu et al. 2010). This is due to the fact that the tensile stress field that develops around the indentation impression reaches the critical value for crack nucleation. Since indentation testing is a convenient method to probe the mechanical properties of materials compared to other mechanical testing methods, such as fracture mechanics testing under tensile or bending loading, the ability to evaluate HE cracking upon indentation is of importance.

In addition, indentation test induces permanent impression crater, which is similar with shot peening. Peening techniques make the material harder but in addition also introduce compressive residual stress. It is well known that compressive stress is effective in preventing HE cracking. With multiple shot impacts on the surface, the surface hardened layer expands plastically and compressive residual stress develops (Kobayashi et al. 1998). However, the boundary of the peening area (outside the crater) sometimes shows tensile stress (Klemenza et al. 2009). This could lead to

mechanical degradation such as HE, stress corrosion cracking (SCC), and fatigue fracture. In fact, a single crater (permanent impression due to indentation) forms tensile stress around the impression, balanced by local compressive strain. Such a tensile stress may induce HE cracking, experienced in high-strength steels (Yonezu et al. 2010, 2012).

From the above engineering background, indentation method may bring the possibility to characterize HE cracking. In this review, the first topic is to explore the use of Vickers indentation testing for evaluating the susceptibility of steel to HE cracking. For this purpose, indentation test is applied to hydrogen-charged steel. The resistance to crack propagation, in particular, the threshold stress intensity factor (K_{ISCC}), is an important parameter for understanding the susceptibility to HE cracking. The second topic is to clarify HE cracking produced by residual stress of indentation impression. For this experiment, spherical impression crater is exposed in hydrogen environment, and HE cracking morphology and the mechanics are systematically investigated. This may become a potential fracture mode, when the steel forms a permanent crater on the surface due to surface treatment (e.g., shot peening) or other types of contact loading in a hydrogen environment. It is expected that the present knowledge is of importance and will significantly contribute to material/mechanical design in a hydrogen environment. In addition, the findings (of the first topic) allowed us to propose an alternative method to the fracture mechanics approach for HE cracking evaluation.

Evaluation of Threshold Stress Intensity Factor for HE Cracking

Materials and Experimental Methods

The material used in the present study was 18Ni maraging steel (350 ksi), which is a low-carbon martensitic steel. In order to achieve high strength, the steel was solution heat treated (820 °C for 3 h) followed by cooling in air to room temperature. Subsequently, the steel was aged at 500 °C for 4 h and air-cooled to room temperature. The mechanical properties of the steel are shown in Table 1, indicating that the yield stress and tensile strength were 2.40 and 2.45 GPa, respectively (Boyer and Gall 1985).

This steel has superior tensile strength, but is very susceptible to hydrogen embrittlement (Gangloff and Wei 1974; Pao and Wei 1977; Antlovich et al. 1980;

Table 1 Mechanical properties of 18Ni maraging steel (350ksi) employed in this study

Young's modulus E (GPa)	Poisson's ratioν	Yield strength σ_y (GPa)	Tensile strength σ_B (GPa)	Work hardening coefficient n	Strength for HE cracking σ_{scc} (GPa)
210	0.3	2.4[a]	2.45[a]	0.025	0.65[b]

[a]Boyer and Gall (1985) Metals Handbook
[b]Yonezu et al. (2010)

Reddy et al. 1992; Gangloff 2003; Tsay et al. 2005, 2008). The specimens in the study were disk-shaped plates with a diameter of 20 mm and thickness of 1 mm. After mechanically and electrochemically polishing the specimen surface, cathodic charging was carried out in order to introduce hydrogen into the material in a buffer solution of sodium acetate (0.20 mol/L CH_3COOH + 0.17 mol/L CH_3COONa, pH = 4.7) with a current density of 3 A/m^2. In order to vary the hydrogen content in the steel, the duration of hydrogen charging was varied from 48 to 72 h.

After cathodic charging, the total diffusible hydrogen content in the material was measured by thermal desorption spectroscopy (TDS-KU, ULVAC). Just after the cathodic charging, TDS measurements indicated C_H to be 33.7 ppm for 48-h charging and 49.1 ppm for 72-h charging. When the specimen with absorbed hydrogen is conditioned in air at room temperature, the hydrogen in the material diffuses out into the atmosphere as a function of the exposure time (degassing time). This suggests that C_H can be controlled by changing the degassing time. The discharged C_H as a function of conditioning time was also measured by TDS, indicating that the C_H for both specimens decreased with increasing degassing time (C_H was varied from 49.1 to almost 0 ppm). By referring to this hydrogen degassing behavior, the timing of the indentation test can be determined at a desired C_H in order to examine the relationship between the HE susceptibility and the C_H.

Indentation testing was carried out using a hydraulic servo-controlled fatigue testing machine equipped with a diamond Vickers indenter. The indenter impresses the specimen surface with up to a specific maximum indentation force at a rate of 1 N/s. Subsequently, the indentation force is reduced at a rate of 1 N/s until $F = 0$ N. The maximum force was varied from 100 to 300 N. The detailed conditions used will be described in each section below. After the indentation test, the impression morphology was observed using an optical microscope. These observations were conducted at least 1 h after the indentation test.

Experimental Results

Vickers indentation was applied to the specimen that had absorbed hydrogen as a result of cathodic charging for 72 h (C_H = 49.1 ppm). Figure 1 shows an optical micrograph of the impression and its surrounding showing that four cracks propagated from the corners of the impression. These are similar to surface cracks (radial and halfpenny-shaped cracks) observed in brittle materials subjected to Vickers indentation (Lawn et al. 1980; Niihara 1983; Cook and Pharr 1990). We previously reported that the cracks grew in a zigzag manner, indicating that they propagate along grain boundaries (Yonezu et al. 2010). Such intergranular cracks are often observed in maraging steel when subjected to hydrogen embrittlement (Gangloff 2003; Tsay et al. 2005, 2008). Furthermore, from observations of cross-sectional views, each crack was identified as a type of radial crack, which propagates along the radial direction from one corner of the indentation impression (Yonezu et al. 2010). In contrast, steel with no hydrogen absorption (as-received specimen: C_H less than 0.05 ppm) did not exhibit any cracking around the impression. We thus

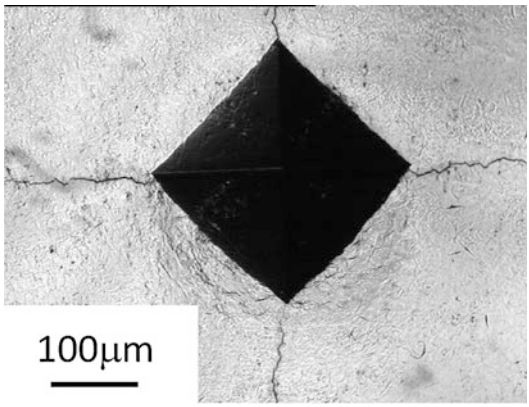

Fig. 1 Micrographs of the indent impression produced in a hydrogen-charged specimen tested with $F_{max} = 300$ N (hydrogen content is 49.1 ppm)

concluded that the crack formation in the present case was caused by hydrogen embrittlement (Yonezu et al. 2010).

Figure 2 shows the relationship between the surface crack length and the maximum indentation force. Here, the tested specimens were charged for 72 h, and all specimens had C_H of 49.1 ppm. The crack length (designed as c) is defined as the distance from the impression corner to the crack tip. The number of tests with $F_{max} = 100$, 200 and 300 N were three, five and nine, respectively. Their standard deviations are also plotted in the figure. It should be noted that for one indentation impression, the number of cracks formed was usually four (such as seen in Fig. 1). However, in some impressions (especially those produced with a smaller $F_{max} = 100$ N), the number of cracks tended to be two or three. Thus, the representative crack length for one test was assumed to be the averaged value, that is, the sum of the crack lengths divided by the number of cracks formed. Figure 2 reveals that the crack length c increases when F_{max} is larger. Figure 2 also shows the results for half of the diagonal length in the impression (designed as a) as a function of F_{max}, also indicating that the impression size is larger with increasing F_{max}.

In order to investigate the effect of hydrogen content on the crack size, indentation tests were conducted at different times after cathodic charging for 72 h. The value of F_{max} was set at 300 N for all tests. Figure 3 shows three micrographs of representative surface cracks in specimens with different hydrogen content which propagated from the impression corners; the tests were conducted at different discharge times (0 h (a), 43 h (b), and 119 h (c)) for hydrogen contents of 49.1, 26.9, and 19.5 ppm. Although F_{max} was set at the same value (300 N) for all the tests, the crack length was strongly dependent on C_H, showing that the length became longer when C_H was larger.

Figure 4 shows the crack length as a function of C_H for all specimens. Here, the specimens with $C_H > 20$ ppm were obtained from 72-h cathodic charging, while the results for C_H around 5 ppm were obtained from the 48-h charging specimen. It can be seen that the crack length became larger with increasing C_H. Figure 4 also shows the Vickers hardness values measured from the impression size (marked

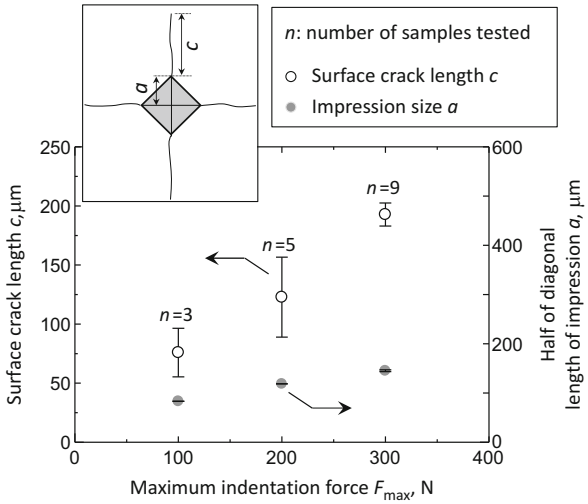

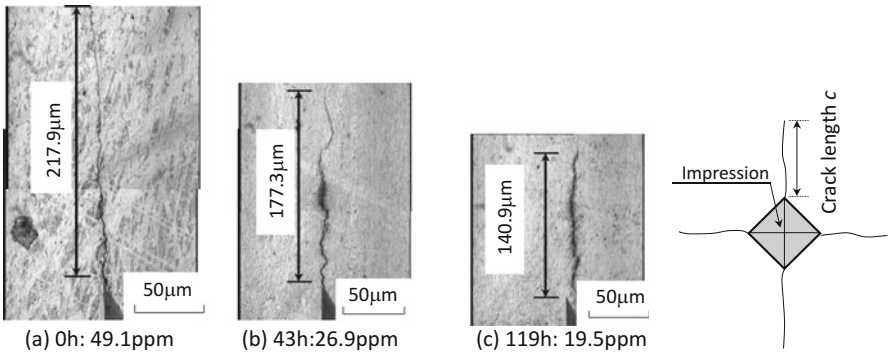

Fig. 2 Variations in crack length and impression size as a function of maximum indentation force

Fig. 3 Micrographs of the crack produced from an indent impression corner tested with $F_{max} = 300$ N. Three tests were conducted at different times after the hydrogen charging: (**a**) 0 h, (**b**) 43 h, and (**c**) 119 h. The hydrogen content was estimated to be (**a**) 49.1, (**b**) 26.9, and (**c**) 19.5 ppm

by a gray circle). The hardness did not depend on the C_H and showed an almost constant value equal to the hardness of the as-received steel with no hydrogen absorption ($HV = 675$) as indicated by the dotted line. Therefore, it is concluded that hydrogen in the steel influences the propagation of the Vickers indentation-induced crack, while the hardness related to the macroscopic elastoplastic properties in compression is not affected by the presence of hydrogen in the steel. Thus, hydrogen in the steel causes a decrease in the critical tensile strength, resulting in HE crack initiation and propagation. Propagation of the crack tip is expected to be suspended upon full unloading under the stress state, where the driving force of the crack propagation (due to the residual stress field from the indent formation) is equilibrated with the resistance to crack growth in the steel having hydrogen.

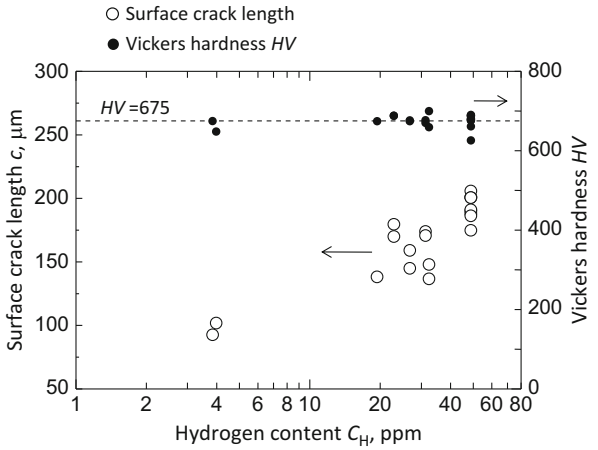

Fig. 4 Variations in radial surface crack length and Vickers hardness as a function of hydrogen content

In other words, the "final" crack length is dependent on resistance to HE crack propagation in the material.

Here, several questions regarding crack propagation arise, such as how the crack grows, what the growth rate is, and when crack propagation stops. In fact, K_{ISCC} tests based on fracture mechanics show that an HE crack starts to propagate when the stress intensity exceeds K_{ISCC} (the threshold resistance to HE crack growth), the growth rate rapidly increases, and the crack propagates stably at the constant crack growth rate (so-called plateau region). Finally, unstable fracture occurs at around K_{IC}. This implies that K_{ISCC} is much lower than K_{IC}. In other words, an HE crack cannot propagate when the stress intensity factor is lower than K_{ISCC}.

In our indentation tests, the total testing time (including both loading and unloading) was about 600 s, for the test condition of $F_{max} = 300$ N and loading rate of $dF/dt = 1$ N/s. If the crack initiates and propagates up to a length of 200 μm (see Fig. 3) during the indentation test, the average rate of crack growth may be about 3.33×10^{-7} m/s. In contrast, fracture mechanics tests yielded HE crack growth rates in the plateau region for 18Ni-300 (300 ksi grade) and 18Ni-250 (250 ksi grade) maraging steels of 5.0×10^{-5} (Sumitomo Precision Products CO. L.1992) and 1.11×10^{-7} m/s (Gangloff 2003), respectively. These values are of the same order as the average rate in the present study. This implies that the HE crack propagation due to indentation corresponds to the plateau region, indicating that the crack grows stably in the present tests.

We will next discuss when the crack stops propagating. Note that the measurement of crack length (in Fig. 3) in the present tests was conducted more than 1 h after the test. Considering the maximum crack length of about 200 μm for $F_{max} = 300$ N (see Fig. 3), assuming the crack continuously propagates until when the microscopic observations were conducted, the average crack growth rate is less

than 6.7×10^{-8} m/s. This value is smaller than the stable rate in the plateau region (5.0×10^{-5} and 1.11×10^{-7} m/s for 18Ni-300 and 18Ni-250 maraging steels as mentioned above), suggesting that the crack in the present study underwent stable propagation. In addition, when we continually observed the crack length up to 100 h after the test, the length did not change. In this case, the crack growth rate was less than about 1.1×10^{-12} m/s, since the measurement resolution of the optical microscope was less than 0.4 μm. This rate is almost the same order as the threshold rate (2.8×10^{-12} m/s), when the value of K_{ISCC} was determined in the fracture mechanics test (Yamaguchi et al. 1997). Therefore, after full unloading, the driving force of the crack tip (stress intensity K) is considered to be less than the value of K_{ISCC}. Such a condition of $K \leq K_{ISCC}$ indicates that the HE crack stops propagating, resulting in the final crack length. In the next section, the stress field at the crack is computed to evaluate the threshold stress intensity of the final crack.

Numerical Analysis

Cohesive Zone Model

The stress field at the crack tip is a key issue, as expected from the above results, since the crack length (at full unloading) is dependent on the HE crack growth resistance of steel, K_{ISCC}. Note that the process of indentation loading/unloading remarkably changes the stress field, resulting in HE crack initiation and propagation (Yonezu et al. 2010). Therefore, such crack growth is required to be incorporated with stress analysis. We employed the finite element method (FEM) to compute the indentation stress field in conjunction with crack propagation.

One of the approaches to simulate crack propagation is the cohesive zone model (CZM). The CZM is theoretically well established and is proven to be applicable to both ductile and brittle materials (Barenblatt 1962; Tvergaard and Hutchinson 1992; Chandra et al. 2002; Xia et al. 2004; Hal et al. 2007; Olden et al. 2008). For instance, Mode-I fracture of a brittle coating on a silicon substrate (Xia et al. 2004), hydrogen embrittlement in a duplex stainless steel (Olden et al. 2008), and the interfacial fracture of an IC-interconnect (e.g., copper and low-K materials) (Hal et al. 2007) have been successfully investigated using the CZM.

Figure 5 shows a schematic of crack propagation incorporating the cohesive zone. The CZM essentially models the fracture process zone in a plane ahead of the crack tip. The zone is assumed to be subjected to cohesive traction. The model usually describes the gradual degradation of the adhesion between two regions along the crack propagation plane. The mechanical response of the cohesive zone obeys a traction-separation law that yields the relationship between the separation distance v of the two material faces at an interface and the traction stress σ acting between them. Figure 5 graphically explains the lumping of the nonlinear material response in the cohesive zone. By the action of the external force (i.e., remote stress/strain), the crack tip opens. The opening response at the actual crack tip (designated as v_B) obeyed the cohesive zone element with the traction-separation law, such as the

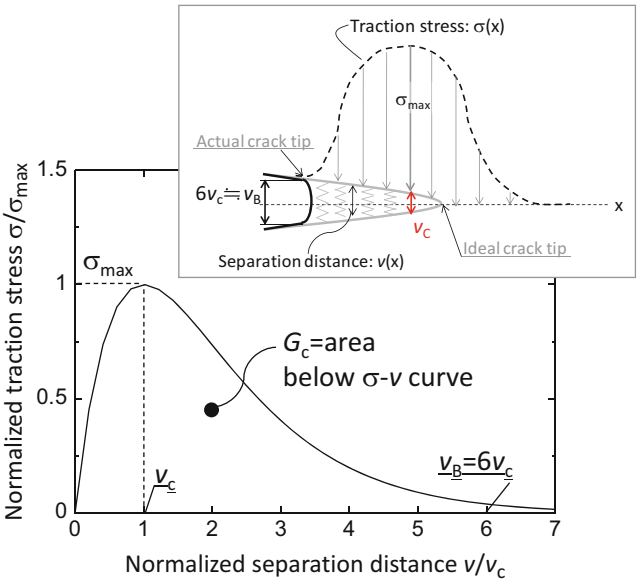

Fig. 5 Schematic of crack advancement with the cohesive zone model. The cohesive zone element having the traction-separation law exists ahead of the crack tip

bottom figure in Fig. 5. In the cohesive zone, after the acting stress σ exceeds the maximum cohesive stress σ_{max} (corresponding to the characteristic separation v_c), the resistance stress (traction force) dramatically decreases to almost zero with larger separation. This indicates that the cohesive zone ahead of the material crack tip opens, and crack propagation then occurs, resulting in the nucleation of new surfaces. Such a simulated crack is permitted to propagate along the specific direction along the cohesive zone element. As shown in Figs. 1 and 3, the surface crack propagates along the radial direction from the indent impression corner. The cohesive element is thus to be inserted in this plane.

Although numerous traction-separation laws for the cohesive zone element have been proposed (e.g., see reference (Chandra et al. 2002) for an overview), an exponential law, called the Smith-Ferrante type (Ortiz and Pandolfi 1999; Hal et al. 2007), is employed due to its simplicity. In fact, the exponential type has been used for various cases, including brittle Mode-I fracture, interfacial delamination, and hydrogen embrittlement cracking (Xia et al. 2004; Hal et al. 2007; Olden et al. 2008) as mentioned above. The constitutive behavior is expressed by the relationship between the normal traction stress σ and corresponding separation distance v across the cohesive element. This is given by

$$\sigma = \sigma_{max} \frac{v}{v_C} \exp\left(1 - \frac{v}{v_C}\right), \tag{1}$$

where σ_{max} is the maximum cohesive stress and v_c is the characteristic opening displacement corresponding to σ_{max} (see Fig. 5). Note that the tangential traction across this surface (i.e., shear component) is ignored in this study, since HE is caused by Mode-I loading and the driving force of the crack initiation and propagation is tensile stress (i.e., principal stress) (Yonezu et al. 2010). For the cohesive zone law, the normal work of fracture G_c corresponds to the area under the traction-separation law, as shown in this figure. It can be described as

$$G_C = \int_0^\infty \sigma(v)\, dv = \exp(1)\sigma_{max} v_C. \tag{2}$$

Therefore, Eqs. (1) and (2) lead to

$$\sigma = \frac{G_C}{{v_C}^2} \exp\left(-\frac{v}{v_C}\right) v. \tag{3}$$

This indicates that the traction-separation curve depends on two variables, the critical energy release rate G_c and v_c (or σ_{max}). When these two variables are known, the traction-separation curve can be drawn.

The critical energy release rate G_c is related to the critical stress intensity factor for crack growth of the material. When considering unstable crack growth, the fracture toughness K_{IC} can be obtained in the plane strain condition as shown below.

$$G_c = \frac{K_{IC}^2}{E}\left(1 - \upsilon^2\right) \tag{4}$$

Here, E and v are the Young's modulus and Poisson's ratio, respectively. As mentioned above, the present study focuses on indentation HE cracking which is expected to be suspended under the condition of the driving force for crack propagation, $K \leq$ threshold stress intensity factor, K_{ISCC}. Thus, in Eq. (4), K_{IC} is hereafter replaced by K_{ISCC}.

Finite Element Method

A three-dimensional model of one-quarter of the specimen was created as shown in Fig. 6. The model contains more than 30,000 nodes and eight-node elements, and the part of the indenter contact and crack propagation (in the cohesive zone element) has a fine mesh. A mesh convergence study was carried out. The calculation was performed using commercially available FEM code (Marc and Mentat 2010.2). A rigid contact surface was used to simulate the rigid Vickers diamond indenter. Coulomb's law of friction was assumed with a friction coefficient of 0.15 (Bowden and Tabor 1950). The indenter penetrated to a maximum force of 300 N and was then withdrawn to zero. The mechanical properties of the as-received maraging steel, listed in Table 1, were used in the FEM computation because the macroscopic

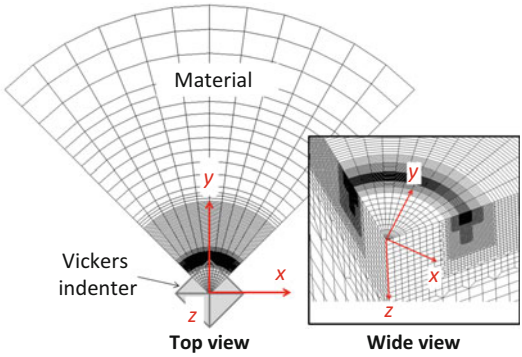

Fig. 6 Stress computation of Vickers indentation with the three-dimensional FEM model

hardness, which is related to the macroscopic plastic properties in compression, does not change with hydrogen content (see Fig. 4).

In order to simulate crack propagation, a cohesive zone element was inserted in the *y*-*z* plane, where the crack extends from the corner of the impression. Thus, during indentation loading/unloading, the simulated crack propagates along the *y*-z plane, and such crack propagation obeys the traction-separation law. We next show computational results for propagation of various cracks. In this study, the actual crack tip is taken as the point where the normal displacement v equals $6v_c$, at which point the normal stress σ on the separated surface is essentially zero (Xia et al. 2004) (see Fig. 5). Since the tensile stress σ_{xx} is responsible for the HE crack propagation, we focused on the distribution of σ_{xx} in this study.

As an example case, the model with crack growth resistance G_c of 108.3 J/m^2 was computed. The maximum stress σ_{max} in Eq. (1) was set to be 0.65 GPa, which was the critical stress for nucleating the present HE crack measured by Vickers indentation (Yonezu et al. 2010). Here, the value of G_c (108.3 J/m^2) for FEM can be converted to a K_{ISCC} value of 5.0 MPa m$^{1/2}$ from Eq. (4). Figure 7 shows a snapshot of the normal stress σ_{xx} distribution at maximum indentation force (a) and upon full unloading (b). For comparison, the model with *no* cohesive zone element was also computed, as shown in Fig. 7c, d. This model simulates the stress field due to indenter contact and does not induce any crack formation: the tensile stress σ_{xx} develops in the elastic field outside the finite plastic deformation region (local impression). Note that the magnitude of σ_{xx} in the fully unloaded condition (Fig. 7d) is higher than that at the maximum indentation force (Fig. 7c). This is because unloading reduces the elastic compressive stress due to the indenter contact, and therefore, σ_{xx} reaches a maximum value at full unloading.

In contrast, in Figs. 7a, b, the model with the cohesive zone element showed the release of tensile stress σ_{xx} (indicated by the dotted line in A) outside the impression (compressive plastic strain field). This is due to crack initiation and propagation. The FEM analysis showed the crack initiated at loading (Fig. 7a) and then propagated significantly under unloading (Fig. 7b). Finally, the crack length reaches a maximum upon full unloading.

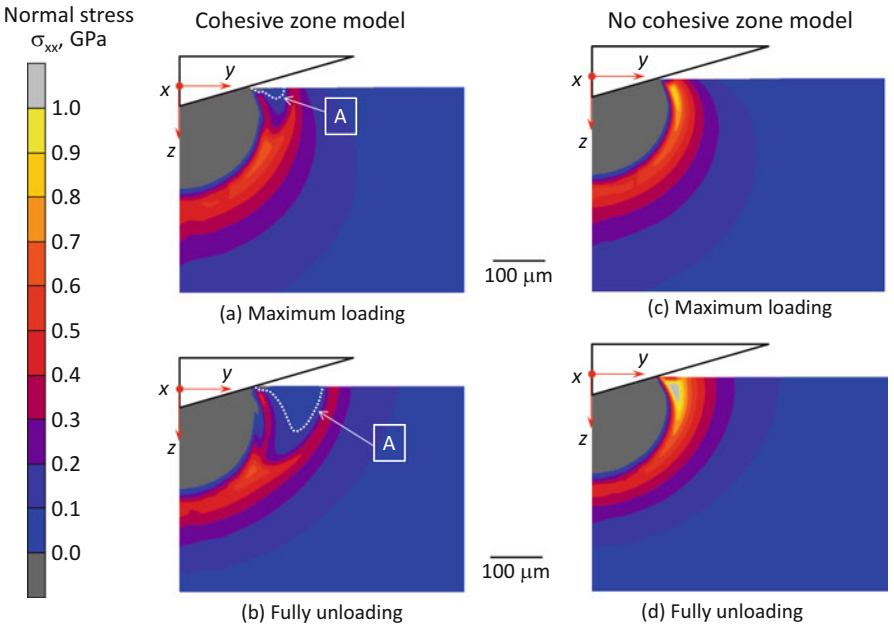

Fig. 7 Contour maps of σ_{xx} for the radial crack with the cohesive zone model (**a**) and (**b**) and without the cohesive zone element (**c**) and (**d**). Note Figs. (**a**) and (**c**) are shown at the maximum indentation force and (**b**) and (**d**) at the end of unloading

Crack Growth Resistance

To evaluate the crack growth resistance of the specimen with C_H of 49.1 ppm, an FEM study was carried out by changing K_{ISCC} from 3 to 8 MPa $m^{1/2}$, in order to analyze the relationship between K_{ISCC} and surface crack length. Here, the FEM model and its constitutive equation for the material were the same as the model described in Fig. 6, and the maximum indentation force was 300 N. Figure 8 shows the relationship between K_{ISCC} and the simulated surface crack length, c, indicating that the crack length is longer with a decrease in K_{ISCC}. The value of $K_{ISCC} \geq 8$ MPa $m^{1/2}$ produced no crack. In this figure, the actual crack length obtained from the indentation experiment (192.7 ± 9.7 μm from Fig. 2) is also shown by the broken line. Here, the thin lines indicate the range obtained from the standard deviation of the experimental results. Compared with the experiments, K_{ISCC} can be estimated to be 4.41 MPa $m^{1/2}$, in the range from 4.28 to 4.55 MPa $m^{1/2}$. It should be emphasized that the variation in the estimated values is not very large, compared with those obtained by the fracture mechanics K_{ISCC} test (Floreen 1978).

To verify the estimated K_{ISCC} obtained from the test with $F_{max} = 300$ N, the other test results with indentation forces of 100 and 200 N were analyzed. Similar to Fig. 9, the experimental crack length (from Fig. 2) was used to estimate the values of K_{ISCC}. The estimated K_{ISCC} gives almost the same value (about 4 MPa $m^{1/2}$ in Fig. 8). As shown in Fig. 3, the impression size as well as the crack length varied

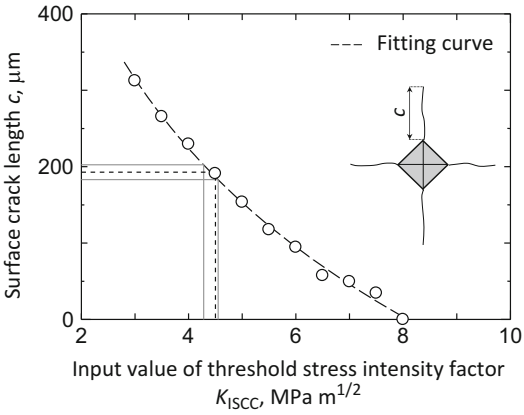

Fig. 8 Variation in crack length during the indentation test computed by FEM incorporating the cohesive zone model

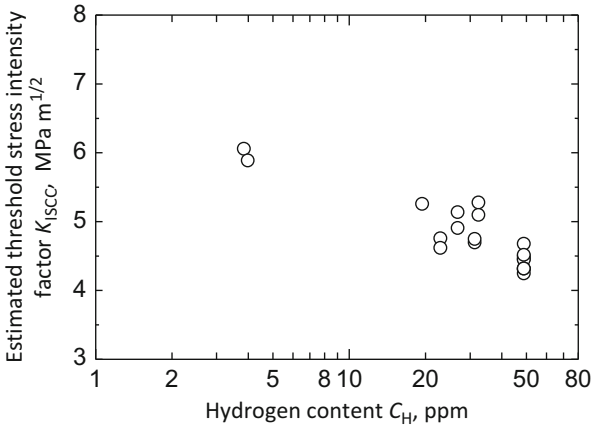

Fig. 9 Estimated threshold stress intensity factor K_{ISCC} as a function of the hydrogen content

depending on F_{max}. This indicates that the stress distribution (which is responsible for crack formation) is different. However, the estimated K_{ISCC} values were almost the same, suggesting that the present estimation is valid.

Figure 9 shows the K_{ISCC} value estimated by the present indentation method as a function of hydrogen content C_H. The K_{ISCC} values were calculated from the data as shown in Fig. 4. This suggests that the estimated values are a function of C_H, indicating that K_{ISCC} is lower with larger C_H. Such a trend was observed in previous studies on HE cracking evaluation for high-strength steels based on the fracture mechanics K_{ISCC} test (Yamaguchi et al. 1997; Gangloff 2003).

Table 2 summarizes the mechanical properties and threshold value of HE crack growth (i.e., threshold stress intensity factor for HE cracking, K_{ISCC}) obtained in the present study together with those for two different grades of maraging steels. The values of K_{ISCC} were obtained by the fracture mechanics test (K_{ISCC} test) in an H_2 environment for 18Ni-250 (250 ksi grade) and in 3.5% NaCl solution for 18Ni-300

Table 2 Comparisons of mechanical properties and threshold stress intensity factor K_{ISCC} among various 18Ni maraging steels

	18Ni maragingsteel grade	Yield stress (GPa)	Tensile strength (GPa)	Fracture toughness (MPa $m^{1/2}$)	K_{ISCC} (MPa $m^{1/2}$)
This study	350ksi	2.4	2.45	40	4.24–6.05[c]
Ref[a]	300ksi	2.07	2.17	75	5.5–11
Ref[b]	250ksi	1.65	1.72	120	20

[a]Sumitomo Precision Products CO, L. 1992, personal communication in 3.5% NaCl
[b]Gangloff (2003), in pressure H_2 ($P_{H2} = 0.17$ MPa)
cK_{ISCC} estimated by the present study

(300 ksi grade) steel. The detailed conditions are described elsewhere (Sumitomo Precision Products CO, L. 1992, personal communication; Gangloff 2003). Since higher strength (higher yield/tensile strength) usually makes the HE susceptibility higher, the value of K_{ISCC} in 300 ksi grade steel is lower than for the 250 ksi grade steel. Our estimation order (4.41–6.05 MPa $m^{1/2}$) is almost the same as the K_{ISCC} values for the other steels (from 5.5 to 11 MPa $m^{1/2}$ for the 300 ksi grade, and 20 MPa $m^{1/2}$ for the 250 ksi grade), although the steel grade and hydrogen content are different. Furthermore, other maraging steels with a yield stress of about 2 GPa were reported to have K_{ISCC} of 10 MPa $m^{1/2}$ (McEvily 1990) and 7.6 MPa $m^{1/2}$ (Floreen 1978), indicating that the values are also close to our estimated values. Thus, this suggests that our method based on indentation can indeed be used to evaluate K_{ISCC}.

Compared with the indentation tests, the fracture mechanics K_{ISCC} test requires much more effort for sample preparation and setting up of the testing method, etc. For instance, the value of K_{ISCC} is usually obtained when crack growth has stopped, with decreasing driving force for crack growth. To recognize the termination of crack propagation, the experiment needs to last a minimum of 1000 h. Thus, the K_{ISCC} test usually requires a long time. In contrast, our method based on indentation saves time and potentially is an alternative technique.

Mechanism of HE Cracking from Indentation Impression

Materials and Experimental Methods

The above section is to investigate whether indentation cracking occurs or not, when the indentation loading is applied to hydrogen-charged steel. On the contrary, indentation cracking from permanent impression due to hydrogen absorption (i.e., when the impression crater is exposed in hydrogen environment) is clarified in this section. We used the same steel, i.e., 18Ni maraging steel (called 350 ksi (Boyer and Gall 1985)), which is a low-carbon martensitic steel. This section used a spherical diamond indenter with a 400 μm radius, which is quite a bit larger than the grain

size of the maraging steel (about 8 μm observed in Yonezu et al. 2010) used in this work. The typical shot peening crater has a diameter of several hundred μm, and in this case, we can ignore the effect of individual crystal plasticity on the stress analysis (based on continuum mechanics). Thus, a relatively large impression crater is required. The maximum indentation forces are 100, 200, and 300 N. The loading rate is set to 1 N/s for all tests, thereby simulating quasi-static contact loading.

After the indentation test to create a permanent impression, cathodic charging was carried out to introduce hydrogen into the material using a phosphate buffer solution (2.6 w/v% K_2HPO_4, 0.2 w/v% NaOH, pH = 6.5) with a current density of 5 A/m^2. In order to vary the hydrogen content in the steel, the duration of hydrogen charging was varied, and two durations of 6 and 48 h were used. The impression morphology was observed using an optical microscope (BXM-N33 M, Olympus Corp.). After the hydrogen charging, the sample was cleaned in ethanol in an ultrasonic cleaner (UT-206, SHARP Corp) for more than 1 h. Some specimens were mechanically cleaned along with fine polishing of buffing in order to remove the oxide film (formed during hydrogen charging) for clear observations. We were able to confirm that the length of the crack did not change before and after the fine polishing to remove the oxide film. Observations of the impression were conducted at least 1 h after the hydrogen charging. We confirmed that the hydrogen crack completely stops propagating after hydrogen charging.

Experimental Results

Indentation tests with different maximum indentation forces of F_{max} = 100, 200 and 300 N were carried out. Cathodic charging of the samples was then carried out for 6 and 48 h. For each test, about 30 impressions were performed. Figure 10 shows optical micrographs of representative indentation impressions and the surrounding area for hydrogen charging of 48 h. These figures separately show the results as a function of hydrogen charging time and F_{max} value. In Fig.10a of F_{max} = 100 N test, the impressions show short cracks (less than about 50 μm) from the rim. Indeed, it is difficult to observe these, since the crack width is very narrow. In Fig.10b of F_{max} = 200 N tests, however, long cracks are clearly observed from the rim. The cracks propagate radially from the impression, indicating a radial crack. Short cracks (similar to Fig.10a) are also observed in these samples. Figure 10c (of F_{max} = 300 N test) show the same trend, indicating two types of cracks. It should be noted that the steel with no hydrogen absorption (before hydrogen charging) did not exhibit any cracking around the indentation impression (Yonezu et al. 2010) (as explained before). The present results indicate that permanent indentation impressions in the steel used absorbed hydrogen-induced short cracks and sometimes long cracks. Although the pictures of 6-h charging tests are omitted, it is found that the crack morphology also changes depending on the hydrogen content and applied indentation force (Niwa et al. 2015).

Figure 11 shows the frequencies of different crack lengths for each test condition. Similar to the series, Figs. 10 and 12 show results separately for different maximum

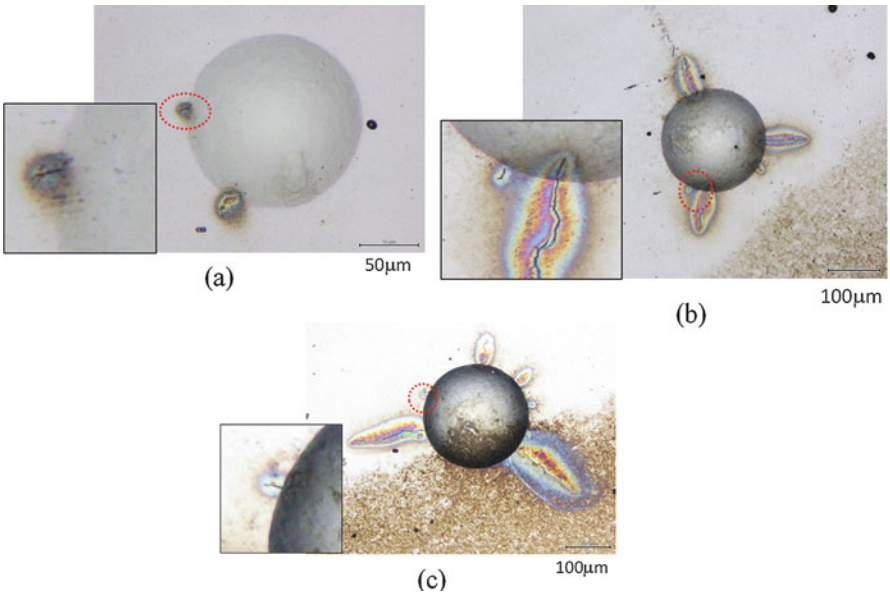

Fig. 10 Micrographs of an impression crater and its surrounding area. The hydrogen charging time is 48 h. The maximum indentation force $F_{max} = 100$ N for (**a**), 200 N for (**b**), and 300 N for (**c**)

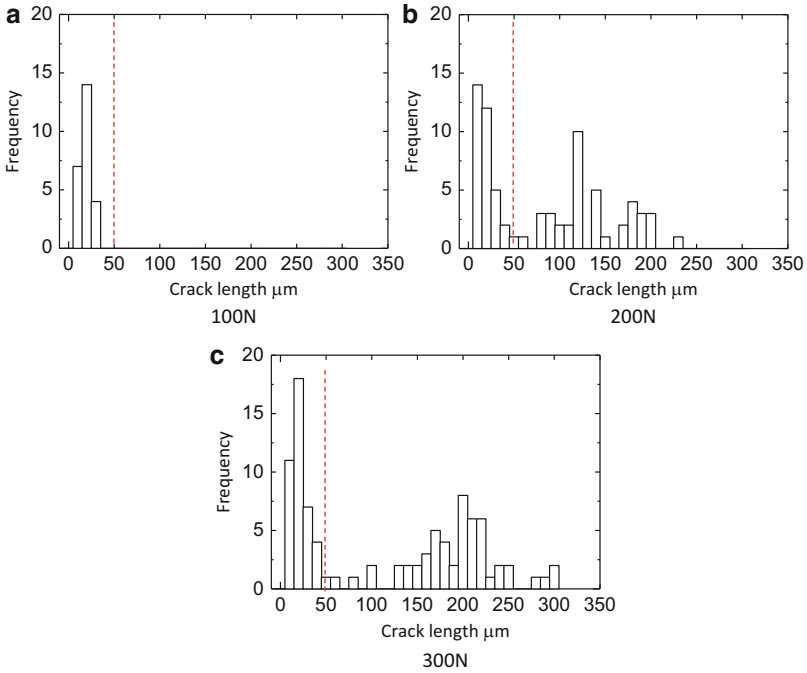

Fig. 11 Frequency of crack lengths from the indentation impressions for $F_{max} = 100$ N (**a**), 200 N (**b**), and 300 N (**c**) (H_2 charging time, 48 h)

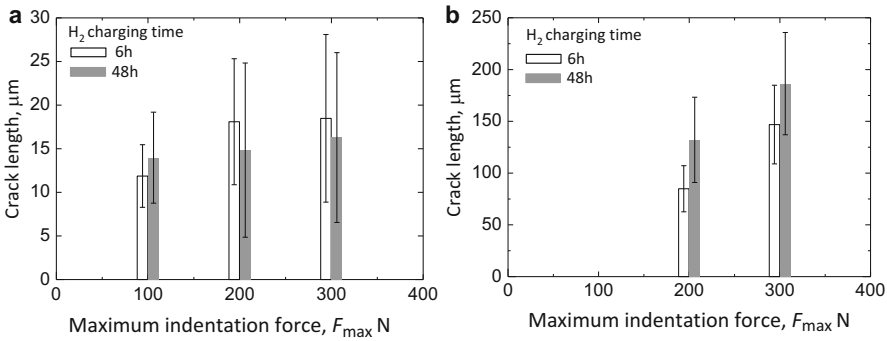

Fig. 12 Changes in crack length (for short cracks (**a**) and long cracks (**b**)) as a function of maximum indentation force

indentation force F_{max} (100, 200, and 300 N). For the $F_{max} = 100$ N test (Fig. 11a), short cracks with length less than 50 μm were observed for both charging times. On the other hand, the tests for $F_{max} = 200$ and 300 N showed two peaks in the distributions, where both short and long cracks exist. As also seen in Fig. 10, the two types of cracks (short and long cracks) can be distinguished, and the boundary between them is set to 50 μm, as shown by the dashed vertical line in Fig. 11.

Subsequently, we measured the crack length for both crack types, as shown in Fig. 12. The short crack length (Fig. 12a) seems to be independent of F_{max} and hydrogen charging time; however, the data shows large scatter. In contrast, Fig. 12b shows that the long crack length has strong dependency on F_{max}. In addition, the crack length is dependent on the hydrogen charging time, and the crack length is longer with larger charging time. The stress distributions and criteria were clarified in the study using finite element simulations, as described in the next section.

Discussion

Mechanism of Crack Propagation

In order to investigate crack formations of Fig. 10, the cohesive zone model (CZM) was employed in FEM to compute the stress field in conjunction with radial crack propagation. As mentioned above (section "Cohesive Zone Model"), this study employed an exponential law (called the Smith-Ferrante law) due to its simplicity. This law requires two independent material parameters, i.e., the maximum stress σ_{max} and the crack growth resistance K_C. The σ_{max} roughly corresponds to the critical stress for crack nucleation. As discussed before, the critical stress (σ_{max}) is estimated to be 0.65 GPa in the present steels which suffer from hydrogen embrittlement (Yonezu et al. 2010, 2012, 2015). In contrast, it is well known that Kc (which is similar to K_{ISCC} as discussed earlier) is strongly dependent hydrogen accumulation (Yamaguchi et al. 1997; Yonezu et al. 2012), and thus K_{ISCC} is not known. In fact, this study explores the actual K_{ISCC} with comparison between the

FEM computation and experiment (see later, section "Crack Length and Stress Intensity Factor").

We created a three-dimensional FEM model of one-quarter of the specimen (similar with Fig. 6). One CZM element for crack propagation is inserted along the center line (at a 45-degree angle from the side surface). It is noted that the situation of crack propagation is different from Fig. 6, because HE crack propagates from permanent impression crater (i.e., crack propagation starts "post" indentation). A permanent impression is first made by spherical indentation with $F_{max} = 100$, 200 and 300 N. After full unloading, the cohesive zone element operates, such that the crack starts propagating. We simulated crack propagation by the residual stress developed around the impression. To make the indenter impression, a rigid spherical indenter was used in a similar manner to that shown in Fig. 6. The mechanical properties used for the FEM are listed in Table 1.

Figure 13 shows representative contour maps of the crack nucleation area upon full unloading. The figure shows cross-sectional views along the crack propagation. For all models, the input value of the stress intensity factor was set to 3.5 MPa $m^{1/2}$, as a representative case. The maximum indentation force was changed to $F_{max} = 300$ N, 200 N, and 100 N, and the results are shown separately in Fig. 13a, b, c, respectively. In the figures, the yellow area indicates the crack nucleation area (i.e., the crack surface). Here, the yellow region defines the crack nucleation area where the CZM interface completely opens, and there is no traction force between the CZM interfaces. It is found that the crack length strongly depends on F_{max}. In particular, the test with $F_{max} = 100$ N produces very small cracks, whose length is about 29 μm (categorized as a "small crack" in this study). On the other hand, the larger F_{max} tests ($F_{max} = 200$ and 300 N) produced long cracks, which were very deep. This computational result corresponds to the experimental results in Figs. 10 and 11.

However, the larger F_{max} tests ($F_{max} = 200$ and 300 N) not only formed long cracks but also small cracks (even if the circumferential stress surrounding the indenter impression was uniform). The question arises as to why two different crack types exist (i.e., the larger F_{max} produces both short and long cracks). The mechanism of such a "multiple crack" scenario was investigated as discussed in the next section.

Mechanism of Multiple Crack Formation

Multiple crack formation with two types of cracks with different lengths was observed, as discussed above. We created a simple FEM model for simulating such a multiple crack propagation. Figure 14 shows a three-dimensional model with half size. Two CZM elements are inserted along the radial direction, so that it can simulate radial crack propagation. Similar to Fig. 13, when the indenter is completely withdrawn, the CZM element starts operating, such that we can simulate crack propagation from the residual stress around the indenter impression. To make the indenter impression, a rigid spherical indenter was used, and the maximum force F_{max} is 300 N. The three-dimensional half model in Fig. 14 comprises 53,200 eight-node elements. The mechanical properties used for the FEM are listed in Table 1.

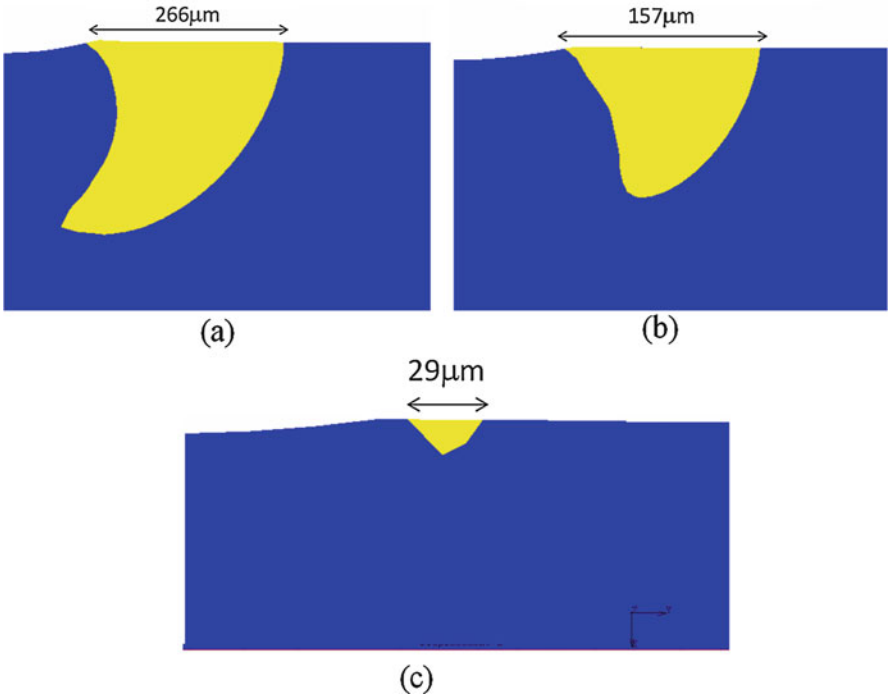

Fig. 13 Contour map of crack nucleation area in the model with $K = 3.5$ MPa $m^{1/2}$. $F_{max} = 300$ N (**a**), 200 N (**b**), and 100 N (**c**)

As shown in Fig. 14, two CZM elements (designated as CZM① and CZM②) are inserted at a certain angle θ. We investigated the relationship between the crack propagation behavior and the crack angle θ, which can be influenced by the interaction of multiple cracks. Indeed, when a crack propagates, the stress around the crack is released, and it may be difficult for a new crack to propagate around that area. However, with increasing distance from the propagated crack, the stress recovers to the original state, resulting in new crack propagation. It should be noted that the distance in this case is the angle in the circumferential direction, and in the present study, this crack angle was set from 30 to 90 degrees, as shown in Fig. 14.

As mentioned above, we experimentally observed the occurrence of both long and short cracks together. In the present case, it seemed that a long crack was generated first, resulting in the surrounding stress field becoming weak. Then, the second crack near the long crack becomes short, while the crack far from the first long one becomes long (i.e., it recovers to the length of the first long crack). The crack length might be dependent on the angle from the first long crack. Based on this assumption, after full unloading, CZM① operates first, followed by the operation of CZM②. Such a "delay" in the computation process is controlled by

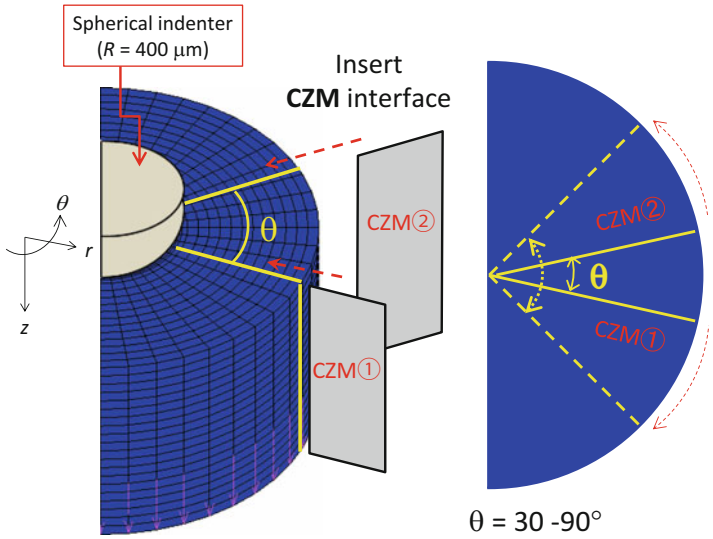

Fig. 14 Three-dimensional FEM model (half model) with cohesive zone element (CZM) for simulating radial crack propagation. This model simulates multiple crack propagation using CZM and CZM whose angle is changed from 30 to 90 degrees

the step increment in the FEM analysis. Of course, if CZM① and CZM② are generated at the same time, their lengths must be the same. In reality, however, it is unlikely to guess that all cracks are generated at the same time during the hydrogen charging, since crack initiation is strongly dependent on both inherent defects (which are present inhomogenously) and the hydrogen accumulation state. Thus, we hypothesize that multiple cracks initiate separately at different times, i.e., CZM① is the "primary crack" and CZM② is the "secondary crack" (in situ monitoring of hydrogen cracking cannot yet be conducted in this study). Note that the material parameters of CZM① and CZM② are identical.

Using the model shown in Fig. 14, we investigated changes in the crack length of CZM① and CZM② as a function of the angle between the two cracks. As a representative case, the threshold stress intensity factor of the crack growth K_{ISCC} was set to 4.5 MPa $m^{1/2}$ for the CZM parameter. Figure 15 shows the results for the computed crack length for two CZM elements. The figure shows top views of the contour map, with the crack propagation area shown as yellow. Figure 15a shows the result for the 30-degree angle, while the result for the 90-degree angle is shown in Fig. 15b. When the angle is 90 degrees (larger angle), the crack lengths of CZM① and CZM② are identical. In contrast, when the angle is 30 degrees, the secondary crack (CZM②) becomes significantly shorter.

We next investigated how the crack length (especially of CZM②) is changed by the angle between the cracks. The results are shown in Fig. 16. It can be seen that the primary crack length of CZM① has little dependence on the angle, while

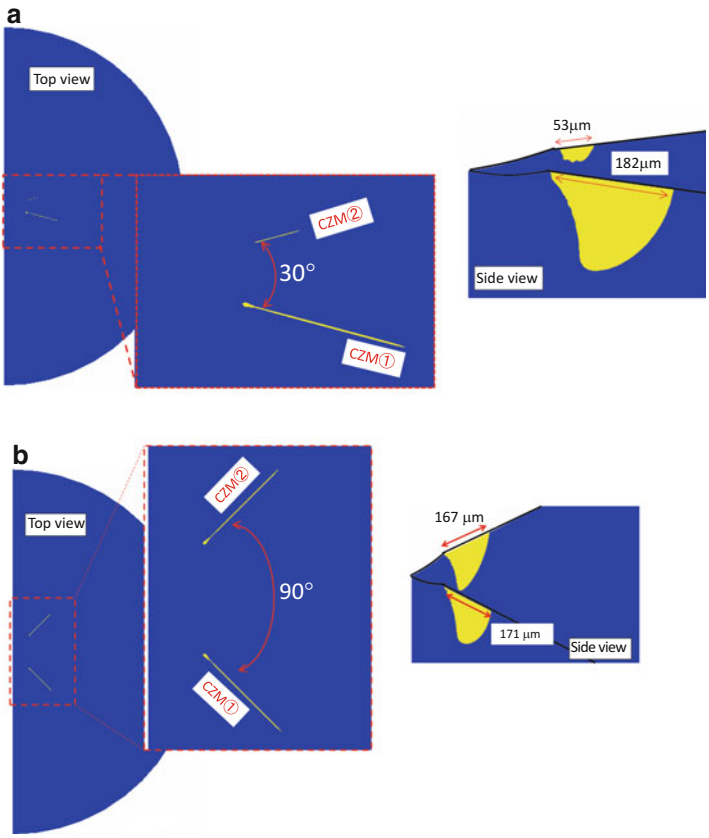

Fig. 15 Contour map of crack nucleation area, showing the multiple crack propagation (crack angle of 30 degrees (**a**) and 90 degrees (**b**))

the secondary crack (CZM②) is strongly dependent on the angle. At an angle of 90 degrees, the length of CZM② agrees well with that of CZM①. This suggests that at 90 degrees, multiple cracks do not interact with each other. However, at a smaller angle (when the position of CZM② is closer to CZM①), the length of CZM becomes significantly shorter. Finally, the length of CZM at about 30 degrees becomes less than 50 μm, and angles smaller than 30 degrees do not produce any cracks in this model. This might be due to the fact that the driving force for the CZM crack becomes small owing to propagation of the primary crack (CZM). Thus, the effect of primary crack generation becomes significant when the crack angle is small. It can therefore be concluded that the above discussion is the mechanism for the appearance of a short crack together with a long crack. It should be noted that this trend (crack length vs. crack angle) is dependent on the crack growth resistance, K_{ISCC}. It is expected that the case of smaller K_{ISCC} leads to a smaller crack angle, while a larger K_{ISCC} leads to a larger angle.

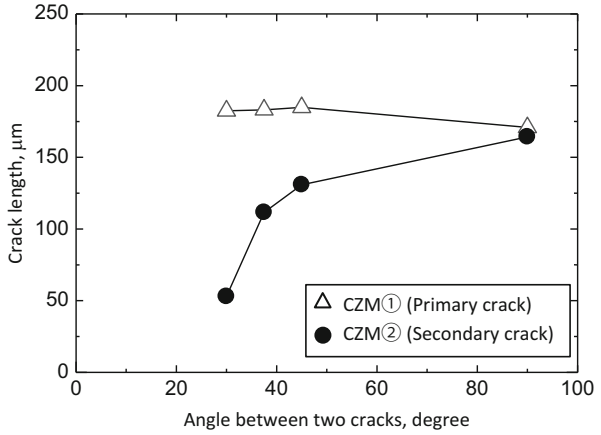

Fig. 16 Simulated crack length with respect to the angle between the two cracks (CZM and CZM)

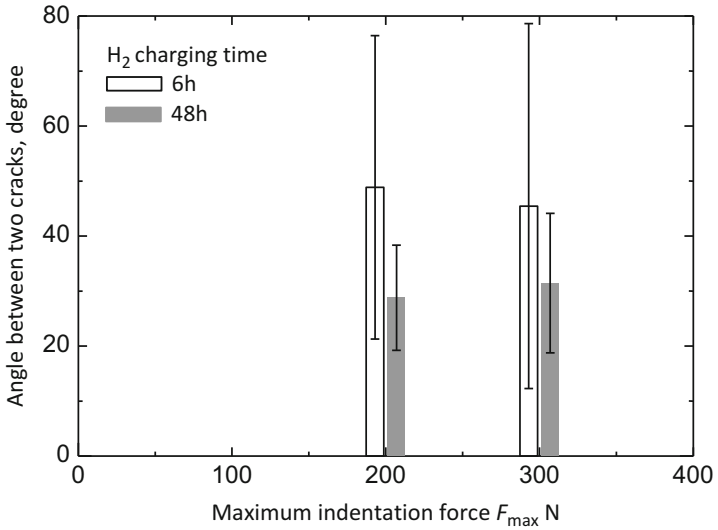

Fig. 17 Experimental result of the angle between the two cracks (short and long cracks)

Experimentally, we measured the angle between the long and short cracks for all indenter impressions. In this study, we only measured the minimum angle between the long and short cracks as the crack angle θ. The results are shown in Fig. 17 as a function of the applied F_{max} and the hydrogen charging time. Although the data show large scatter, the average crack angle θ was about 45 degrees for hydrogen charging for 6 h and 30 degrees for 48-h hydrogen charging. Although θ is dependent on K_{ISCC}, the experimental data are similar to the computational results in Fig. 17, especially for the 48-h charging time (the angle is about 30 degrees).

Crack Length and Stress Intensity Factor

We finally discuss the actual crack length from experimental HE cracking based on stress analysis, especially the stress intensity factor around the crack tip. Here we focus on the "long crack" (see Fig. 16), since it is not influenced by other crack generation. Similar with Fig. 8 of Vickers indentation, we investigated the effect of the input value of the stress intensity factor (crack growth resistance) K_{ISCC} on the crack length. We conducted several computations in this study with various values of the crack growth resistance (stress intensity factor K was changed from 3.0 to 5.5 MPa $m^{1/2}$ in steps of 0.5 MPa $m^{1/2}$) for both the $F_{max} = 200$ N and 300 N tests. As expected, the crack length is strongly dependent on the input K_{ISCC}, indicating that the crack length is longer when K_{ISCC} is smaller (like Fig. 8). In addition, a strong dependence of F_{max} on the crack length was observed, i.e., with larger F_{max}, the radial crack becomes longer. This relationship can yield the actual K_{ISCC} when the crack length is known. Therefore, the experimental crack length is substituted in this relationship in order to estimate the actual K_{ISCC}.

The estimated values are investigated as a function of the maximum indentation force, F_{max}. This indicates that the estimated K_{ISCC} depends on the hydrogen charging time (i.e., hydrogen content), while it is not dependent on F_{max}. For the hydrogen charging time of 6 h, K_{ISCC} is estimated to be 4.9 MPa $m^{1/2}$, while for the charging time of 48 h, K_{ISCC} is 4.3 MPa $m^{1/2}$. As mentioned in section "Crack Growth Resistance," the K_{ISCC} via Vickers indentation is estimated from 4 to 6 MPa $m^{1/2}$ (depending on the hydrogen content). As shown in Table 2, furthermore, fracture mechanics tests for HE cracking reported the values of K_{ISCC} to be in the range of 5.5 to 11 MPa $m^{1/2}$ (although the steel grade and hydrogen content in these tests are different from those in the present study). These values are in reasonable agreement with our estimation, suggesting that the present crack length (long crack) is governed by the threshold stress intensity factor K_{ISCC} for HE. Thus, the present findings may be useful for prediction of HE crack morphology from indentation impression.

Conclusion

This study investigated indentation-induced cracking in a maraging steel due to hydrogen embrittlement (HE). This review addressed two topics. The first one is that Vickers indentation was applied to the hydrogen-charged steel, such that we explored new evaluation method for HE susceptibility. The second topic is to investigate HE crack morphology from the residual stress that develops around a spherical indentation impression crater.

In the first topic, it is discovered that Vickers indentation induces hydrogen embrittlement cracking. The surface crack length is dependent on the hydrogen content in the steel. Since the stress intensity factor is equilibrated with the threshold stress intensity factor, K_{ISCC}, the stress field upon indentation in conjunction with crack growth was computed by the finite element method (FEM) incorporating a cohesive zone model. It was found that the simulated crack starts to grow under

loading and then propagates under unloading. The crack length finally reaches a maximum value at full unloading. The FEM with different values of the crack growth resistance (K_{ISCC}) was used to obtain the relationship between K_{ISCC} and surface crack length. By substituting the actual crack length in the relationship, K_{ISCC} could be estimated. The estimated values were found to agree with the K_{ISCC} values measured by fracture mechanics testing (K_{ISCC} test). Furthermore, our method showed a dependence of hydrogen content on K_{ISCC}. This trend is observed when fracture mechanics K_{ISCC} tests are applied to high-strength steel in a hydrogen environment. Such a HE evaluation is usually conducted by K_{ISCC} tests that require significant effort for specimen preparation and setting up of testing, etc. However, the indentation-based evaluation method proposed in this study is very simple and convenient. The present approach is an alternative for evaluation of HE cracking.

The second topic clarified the stress criterion of hydrogen embrittlement cracking (i.e., HE crack initiation and propagation) from the residual stress of indentation impression. Namely, when spherical impression crater is exposed in hydrogen environment, how HE cracking propagates from the crater was investigated. The HE crack propagates radially, and the crack length is dependent on maximum indentation force and critical crack growth resistance K_{ISCC} (which is changed by the hydrogen content). In addition, a larger indentation force results in a complicated HE fracture, showing both long and short cracks. In this case, the appearance of the short cracks is affected by stress release of a neighboring long crack. These findings in our systematic investigation may be useful to predict damage of HE cracks, produced by residual stress in the permanent impression. Especially, this will be useful to determine how the size of an impinging foreign object (indenter size and shape) and the loading magnitude (maximum indentation force) induce HE damage, including crack length. This may become an indicator for HE upon permanent impression crater/dimple formation, such as by shot peening and localized contact loading.

Acknowledgment We would like to thank Professor Kohji Minoshima (Osaka University) for his guidance. This work is supported by JSPS KAKENHI (Grant No. 22760077 and 26420025) from the Japan Society for the Promotion of Science (JSPS) and Research Grant of Suga Weathering Technology Foundation (SWTF).

References

S.D. Antlovich, T.R. Risbeck, et al., The effect of microstructure on the fracture toughness of 300 and 350 grade maraging steels. Eng. Frac. Mech. **13**, 717–739 (1980)

G.I. Barenblatt, Mathematical theory of equilibrium cracks. Adv. Appl. Mech. **7**, 56–129 (1962)

F.P. Bowden, D. Tabor, *The Friction and Lubrications of Solids* (Oxford University Press, Oxford, 1950)

H.E. Boyer, T.L. Gall, *Metals Handbook Desk Edition Metals Park* (American Society for Metals, Ohio, 1985)

N. Chandra, H. Li, et al., Some issues in the application of cohesive zone models for metallic–ceramic interfaces. Int. J. Solids Struct. **39**, 2827–2855 (2002)

R.F. Cook, G.M. Pharr, Direct observation and analysis of indentation cracking in glasses and ceramics. J. Am. Ceram. Soc. **73**, 787–817 (1990)
S. Floreen, Maraging steels/metals handbook 9th edn. vol 1, in *Properties and Selection: Irons and Steels Metals Park*, (American Society for Metals, Ohio, 1978)
R.P. Gangloff, *Hydrogen Assisted Cracking of High Strength Alloys* (Elsevier Science, New York, 2003)
R.P. Gangloff, R.P. Wei, Gaseous hydrogen assisted crack growth in 18 nickel maraging steels. Scri. Metall. **8**, 661–668 (1974)
B.A.E. Hal, R.H.J. Peerlings, et al., Cohesive zone modeling for structural integrity analysis of IC interconnects. Microelectron. Reliab. **47**, 1251–1261 (2007)
M. Klemenza, V. Schulzea, et al., Application of the FEM for the prediction of the surface layer characteristics after shot peening. J. Mater. Process. Technol. **209**, 4093–4102 (2009)
M. Kobayashi, T. Matsui, et al., Mechanism of creation of compressive residual stress by shot peening. Int. J. Fatigue **20**(5), 351–357 (1998)
B.R. Lawn, A.G. Evans, et al., Elastic/plastic indentation damage in ceramics: the median/radial crack system. J. Am. Ceram. Soc. **63**, 574–580 (1980)
A.J. McEvily, *Atlas of Stress Corrosion and Corrosion Fatigue Curves* (ASM International, Ohio, 1990)
K. Niihara, A fracture mechanics analysis of indentation-induced Palmqvist cracks in ceramics. J. Mater. Sci. Lett. **2**, 221–223 (1983)
M. Niwa, T. Shikama, et al., Mechanism of hydrogen embrittlement cracking produced by residual stress from indentation impression. Mater. Sci. Eng. A **624**, 52–61 (2015)
V. Olden, C. Thaulow, et al., Application of hydrogen influenced cohesive laws in the prediction of hydrogen induced stress cracking in 25% Cr duplex stainless steel. Eng. Fract. Mech. **75**, 2333–2351 (2008)
M. Ortiz, A. Pandolfi, Finite-deformation irreversible cohesive elements for three-dimensional crack-propagation analysis. Int. J. Num. Methods Eng. **44**, 1267–1282 (1999)
P.S. Pao, R.P. Wei, Hydrogen assisted crack growth in 18Ni (300) maraging steel. Scr. Metall. **11**(6), 515–520 (1977)
K.G. Reddy, S. Arumugam, et al., Hydrogen embrittlement of maraging steel. J. Mater. Sci. **27**, 5159–5162 (1992)
L.W. Tsay, Y.F. Hu, et al., Embrittlement of T-200 maraging steel in a hydrogen sulfide solution. Corros. Sci. **47**, 965–976 (2005)
L.W. Tsay, H.L. Lu, et al., The effect of grain size and aging on hydrogen embrittlement of a maraging steel. Corros. Sci. **50**, 2506–2511 (2008)
V. Tvergaard, J.W. Hutchinson, The relation between crack-growth resistance and fracture process parameters in elastic plastic solids. J. Mech. Phys. Solids **40**, 1377–1397 (1992)
Z. Xia, W.A. Curtin, et al., A new method to evaluate the fracture toughness of thin films. Acta Mater. **52**, 3507–3517 (2004)
Y. Yamaguchi, H. Nonaka, et al., Effect of hydrogen content on threshold stress intensity factor in carbon steel in hydrogen-assisted cracking environments. Corrosion-NACE **53**(2), 147–155 (1997)
A. Yonezu, M. Arino, et al., On hydrogen-induced Vickers indentation cracking in high-strength steel. Mech. Res. Comm. **37**, 230–234 (2010)
A. Yonezu, T. Hara, et al., Evaluation of threshold stress intensity factor of hydrogen embrittlement cracking by indentation testing. Mater. Sci. Eng. A **531**(1), 147–154 (2012)
A. Yonezu, M. Niwa, et al., Characterization of hydrogen-induced contact fracture in high strength steel. J. Eng. Mater. Technol. **137**, 021007 (2015)